



Radar Systems and
Remote Sensing Laboratory

**ULTRA-WIDEBAND RADAR MEASUREMENTS
OVER BARE, SNOW-COVERED AND PANCAKE ICE**

19970801 025

THE UNIVERSITY OF KANSAS CENTER FOR RESEARCH, INC.

2291 Irving Hill Road
Lawrence, Kansas 66045-2969

**ULTRA-WIDEBAND RADAR MEASUREMENTS
OVER BARE, SNOW-COVERED AND PANCAKE ICE**

P. Kanagaratnam¹, S. Gogineni¹, K. Jezek²
L. Peters³, J. Young³, and I. Zabel⁴

¹Radar Systems and Remote Sensing Laboratory, University of Kansas Center for Research, Inc.
2291 Irving Hill Road, Lawrence, Kansas 66045-2969, USA
913/864-4835 * Fax, 913/864-7789 * graham@rsl.ukans.edu

²Byrd Polar Research Center, The Ohio State University
108 Scott Hall, 1090 Carmack Road, Columbus OH 43210-1002
614/292-7973 * Fax 614/292-4697 * jezek@icebergmps.ohio-state.edu

³Electroscience Lab, The Ohio State University
1320 Kinnear Road, Columbus OH 43212
614/292-6153

⁴Lincoln Laboratory, MIT, 244 Wood Street, Lexington MA 02173-9108
617/981-2732 * Fax 617/981-3905 * zabel@ll.mit.edu

RSL Technical Report 12100-1

July 1997

DISTRIBUTION STATEMENT A

Approved for public release
Distribution Unlimited

Sponsored by:

Office of Naval Research, 800 N Quincy St, Arlington VA 22217-5660
Document no. N00014-96-1-0219

1. Introduction

An ultra-wideband radar and a plane-wave antenna have been used to measure the high-resolution scattering response of bare saline ice, snow-covered ice and pancake ice during the winter seasons of 1994 and 1995 at the US Army Cold Regions Research and Engineering Laboratory (CRREL). The objectives of these experiments were to study various mechanisms for simulating roughness and to understand scattering mechanisms better.

These backscatter measurements were made at 2-18 GHz and 0.5-16.5 GHz during the 1994 and 1995 experiments, respectively, and were made for incidence angles ranging from 0° to 55° . These broadband measurements provide a vigorous test for models at many frequencies using a single system instead of many single-frequency systems.

2. The Plane-Wave System

In order to perform broadband scattering measurements, we developed a network-analyzer-based ultra-wideband (UWB) radar using a compact range antenna. This system, as well as providing exceptional range resolution, also provides excellent angular resolution because of the plane waves generated by the compact range antenna [Gogineni et al., 1995]. Previous radar systems using horn antennas had beamwidths in the range of 6° to 20° , which made it difficult to determine the scattering mechanisms from distributed targets as a function of incidence angle. With high range resolution, on

the order of centimeters, we were able to resolve the reflections from the complex ice layers, which was never accomplished before.

2.1 Compact Range Antenna

To obtain better resolving capability and angular response from saline ice we used a compact range antenna with a wideband (2- to 18-GHz) network-analyzer-based radar. Previous radar systems used antennas whose illumination of the distributed target contained a wide range of incidence angles, which made it difficult to determine primary scattering sources. Figure 2.1 shows a comparison between the plane-wave system and conventional systems.

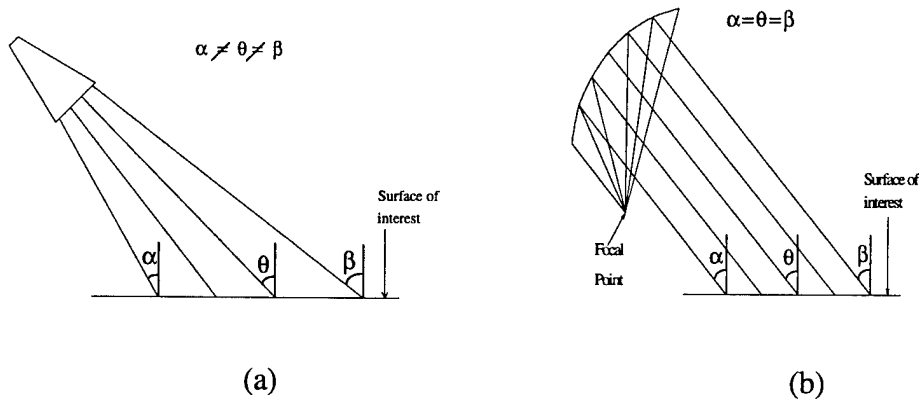


Figure 2.1. (a) Conventional radar systems. (b) Plane-wave system.

A 42-inch-diameter parabolic reflector antenna was used to transform spherical waveforms from the offset AEL horn feed antenna into plane waves of uniform phase over an area approximately equal to the area of the reflector and at ranges up to $0.5*D^2/\lambda$, where D is the reflector diameter and λ is the wavelength. The feed was

adjusted to place the phase center of the feed at the focal point of the reflector. Both vertically and horizontally polarized measurements can be made with this system by properly orienting the feed. The rims of the reflector and the feed support were covered with echosorb to minimize the distortion of the incident plane wave and to reduce the scattering from these objects. Figure 2.2 shows the field of the plane wave. The distance indicated in the figure is relative to the edge of the parabolic dish.

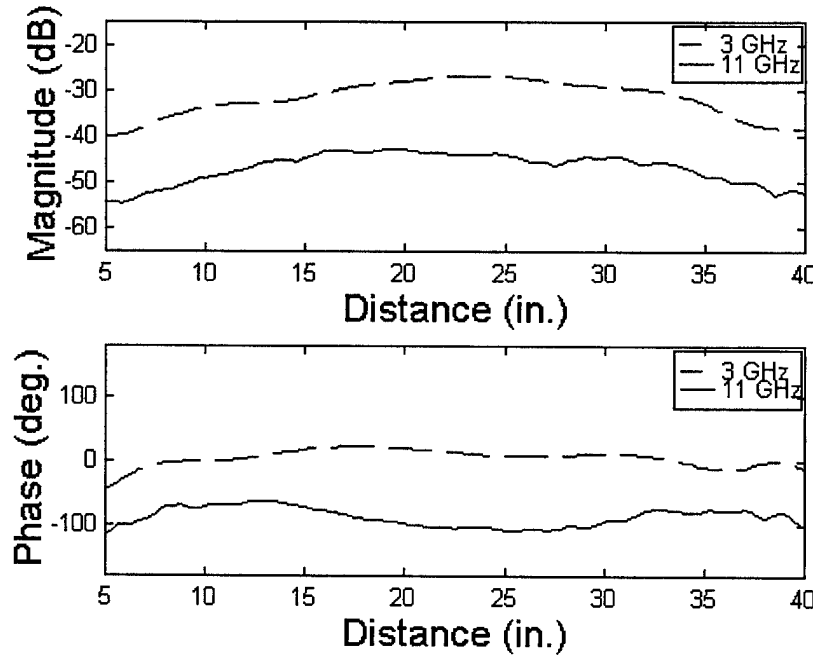


Figure 2.2. Field of plane wave 6 feet away from the antenna shown for 1995 system.

2.2 Step-Frequency Radar

The step-frequency radar [Izuka et al., 1984] was used together with the compact range antenna to measure the scattering coefficient of young saline ice. The main feature of the step-frequency radar is the high resolution that can be obtained by

exploiting the phase property of the signal. The transmitter signal is stepped in frequency beginning over the desired bandwidth, and the amplitude and phase of the received signal are measured at each frequency. The measured data are concatenated and Fourier-transformed to obtain the impulse response of the target. The power return as a function of frequency is obtained by range gating to isolate the return from clutter and taking the inverse Fourier transform.

2.2.1 Description

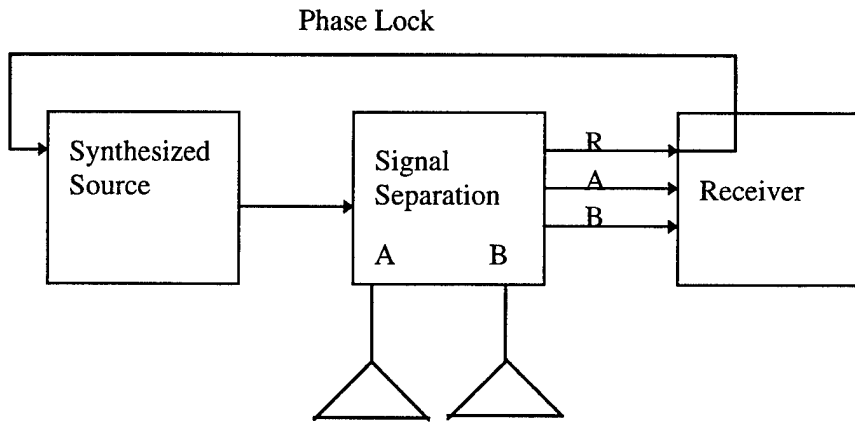


Figure 2.3. Block diagram of network-analyzer-based step-frequency radar.

The figure above shows a simple block diagram of the network-analyzer-based step-frequency radar used in our experiments. The synthesized source can generate a swept signal in the range of 50 MHz to 40 GHz. The start-and-stop frequency can be easily selected within this range via software. To achieve high frequency accuracy, a portion of the source signal is routed to the R sampler in the receiver and routed back to the source for phase locking. The signal separation device consists of a power splitter, two directional couplers and a transfer switch. The power splitter couples some of the

incident signal to the R sampler for phase locking and reference. The transfer switch is used to switch between measurements in the forward direction (S_{11} and S_{21}) and reverse direction (S_{22} and S_{12}). The directional couplers couple the reflected signal from the target to the A sampler in the receiver for S_{11} measurement and to the B sampler for S_{21} measurements when the transfer switch is set in the forward direction. The receiver then downconverts the received signal to IF.

In the experiments that we conducted, the frequency of the network analyzer was stepped through 16 GHz of bandwidth (2-18 GHz in 1994 and 0.5-16.5 GHz in 1995) in 10-MHz steps resulting in 0.94-cm range resolution. Figure 2.4 shows the system configuration of the ultra-wideband (UWB) radar system. Scattering measurements were made in S_{11} mode with this system at an outdoor saline pond at the CRREL facility in Hanover, New Hampshire.

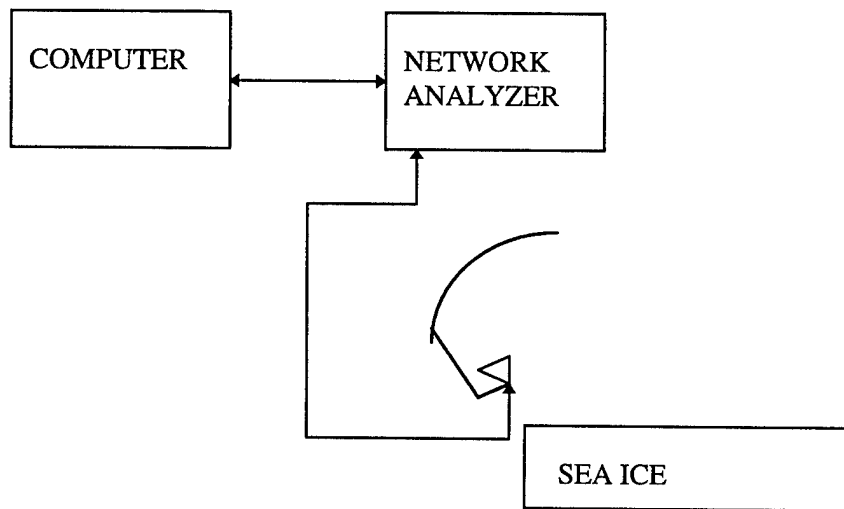


Figure 2.4. Setup of the UWB radar-compact range antenna system.

3. US Army Cold Regions Research and Engineering Laboratory Experiment (CRRELEX) Description

To understand the backscatter mechanisms of sea ice, radar backscatter measurements were performed on artificially grown sea ice in an indoor facility at the US Army Cold Regions Research and Engineering Laboratory (CRREL) during the 1994 and 1995 winter seasons. The frozen pond was made with saline water in order to simulate sea ice. The pond is about 15m wide by 20m long. The facility has a catwalk on railroad tracks that were used to place the antenna mount, the network analyzer and the data acquisition system. The mobility of the catwalk permitted us to obtain four independent samples at each angle and also make 200 independent measurements at a fixed angle for probability density function (pdf) calculations.

In January 1994, measurements were made on bare ice and snow-covered ice at incidence angles ranging from 0° to 55° with VV polarization. Pdf measurements were also made on this ice at nadir. In March 1994, measurements were made on bare ice and snow-covered ice at incidence angles ranging from 0° to 60° with VV and HH polarizations. In January 1995, measurements were made on pancake ice at incidence angles ranging from 0° to 50° with VV and HH polarizations. Pdf measurements were also made on the pancake ice at 0° and 23° . To create pancake ice, waves were generated on open water with a motorized paddle. The wave action caused the formation of frazil ice first, and this slowly grew to pancake ice during freeze-up.

The tables below summarize the measurements made during these experiments.

Table 3.1. CRRELEX '94 January Data Summary

Date	Angles	Number of Spots	Ice Type	Polarization	Frequency
8 Jan	0°-55°	3	Snow-covered ice	VV	2 - 18 GHz
9 Jan	0°-55°	2	Snow-covered ice	VV	2 - 18 GHz
9 Jan	0°-55°	2	Bare ice	VV	2 - 18 GHz
10 Jan	0°-55°	2	Snow-covered ice	VV	2 - 18 GHz
10 Jan	0°-55°	2	Bare ice	VV	2 - 18 GHz
11 Jan	0°	133 (Pdf)	Snow-covered ice	VV	2 - 18 GHz
12 Jan	0°	103 (Pdf)	Bare ice	VV	2 - 18 GHz
14 Jan	0°	128 (Pdf)	Rough ice	VV	2 - 18 GHz
14 Jan	0°-55°	4	Rough ice	VV	2 - 18 GHz
15 Jan	0°	95 (Pdf)	Snow-covered ice	VV	2 - 18 GHz
15 Jan	0°-50°	4	Snow-covered ice	VV	2 - 18 GHz
15 Jan	0°-50°	6	Rough ice	VV	2 - 18 GHz
15 Jan	0°	126 (Pdf)	Rough ice	VV	2 - 18 GHz
16 Jan	0°	108 (Pdf)	Bare ice	VV	2 - 18 GHz

Table 3.2. CRRELEX '94 March Data Summary

Date	Angles	Number of Spots	Ice Type	Polarization	Frequency
11 Mar	0° - 60°	4	Snow-covered ice	VV & HH	2 - 18 GHz
12 Mar	0° - 60°	4	Bare ice	VV & HH	2 - 18 GHz

Table 3.3. CRRELEX '95 Data Summary

Date	Angles	Number of Spots	Ice Type	Pol.	Frequency
5 Jan	0°-50°	4	Bare ice	VV	1 - 16 GHz
7 Jan	0°-40°	4	Snow-covered ice	VV	0.5- 16.5 GHz
8 Jan *	20°	3	Snow-covered ice	VV	0.5- 16.5 GHz
9 Jan *	17°,23°, 31°,41°,44°,50°	1	Bare ice	VV	2 - 18 GHz
10 & 11 Jan	0°-50°	3	Open water to Pancake ice	VV	0.5- 16.5 GHz
23 Jan	0°-50°	4	Pancake ice	VV	0.5- 16.5 GHz
24 Jan	0°	200 (Pdf)	Pancake ice	VV	0.5 - 16.5 GHz
25 Jan	0°-50°	4	Pancake ice	VV & HH	0.5 - 16.5 GHz
25 Jan	23°	200 (Pdf)	Pancake ice	VV	0.5 - 16.5 GHz

* Bistatic Measurements

4. Signal Processing of the Ultra-Wideband Radar Data

The primary parameter to be extracted from our measurements is the backscattering coefficient of the simulated sea ice as a function of the incidence angle and frequency. The radar equation for the plane-wave system is

$$\sigma^o = \frac{P_r \sigma_{cal} A_{cal}}{P_{cal} A_{ill}} \quad (4.1)$$

where σ^o is the backscattering coefficient of the ice,

P_r is the power returned from the ice,

P_{cal} is the return power from a target of known radar cross section, σ_{cal} ,

A_{ill} is the area illuminated by the antenna on the target, and

A_{cal} is the area illuminated by antenna on the calibration target.

This equation differs from the conventional radar equation because of the absence of range dependence for the plane wave. The radar equation for the plane wave system is independent of range because of its narrow beamwidth. To compute the illuminated area, we first have to determine the distance between the center of the field (similar to those in figure 2.2) and the point where the magnitude falls off by 6 dB for both the horizontal and vertical fields over the frequencies of operation. The distance between the 6-dB points is the distance used in the illuminated area calculations (4.2). The vertical and horizontal fields have been measured in the near-field region (6 ft.) from 1 to 20 GHz in steps of 1 GHz for both vertical and horizontal polarizations at The Ohio State University [Nassar, 1992]. The horizontal and the vertical distances in meters are shown in figure 4.1(a-d) for the antennas used during the 1994 and 1995

CRREL experiments. The distances have been fitted with a linear fit to interpolate for frequencies at which the patterns were not measured. The vertical diameter for the illuminated area is also modified by the incidence angle. Hence, the illuminated area is

$$A_{ill}(f) = \frac{\pi D_V(f) D_H(f)}{4 \cos(\theta)} \quad (4.2)$$

where $D_V(f)$ is the vertical diameter,

$D_H(f)$ is the horizontal diameter, and

θ is the incidence angle.

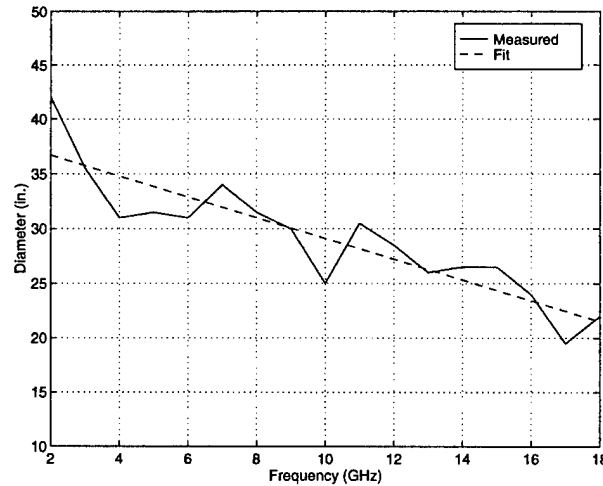


Figure 4.1(a). Horizontal diameter used for illuminated area calculation in 1994.

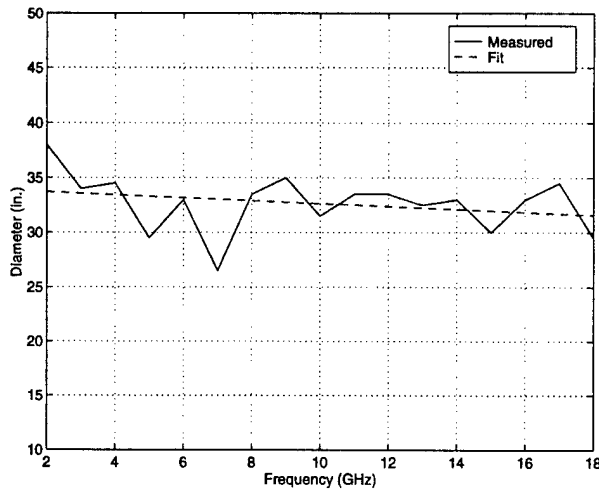


Figure 4.1(b). Vertical diameter used for illuminated area calculation in 1994.

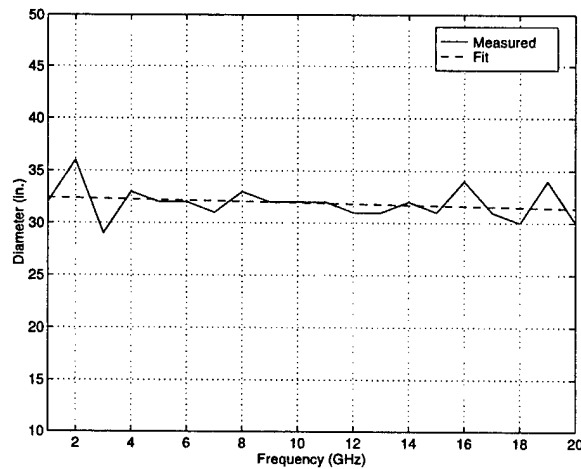


Figure 4.1(c). Horizontal diameter used for illuminated area calculation in 1995.

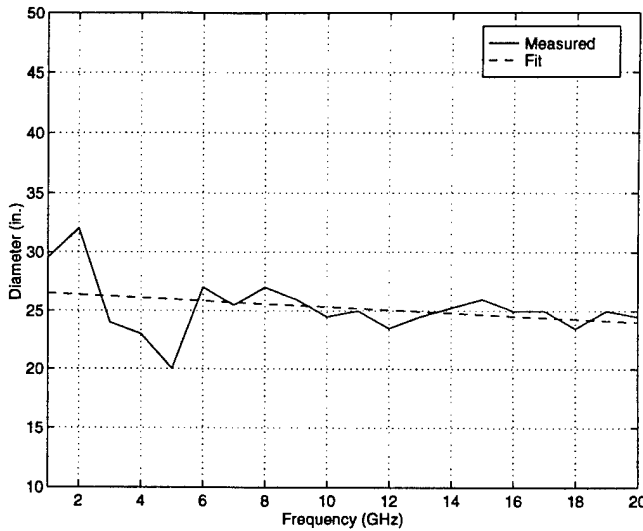


Figure 4.1(d). Vertical diameter used for illuminated area calculation in 1995.

To extract the scattering coefficient of the ice, we need first to determine the return power as a function of frequency. The chart in figure 4.2 below illustrates the steps involved in extracting the frequency response of the return from ice, $P_r(f)$.

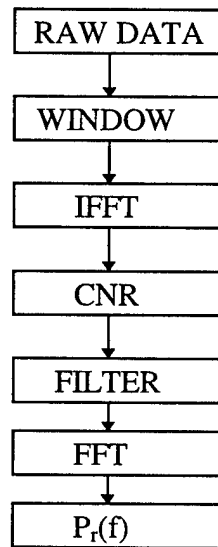


Figure 4.2. Data processing steps to extract frequency response of return from ice.

To determine the location of our target, we need first to obtain the high-resolution spectrum of our data. In the estimation of a spectrum, there are a variety of windows that we can choose to minimize leakage. Unfortunately most conventional windows that have good leakage resistance usually suffer from poor resolution. David J. Thomson [1982] introduced a technique of estimating high-resolution spectra using multiple windows. These windows are optimum in the sense of maximizing the concentration of signal energy within a specified bandwidth, W . The windows are discrete prolate spheroidal sequences (DPSS, also known as Slepian sequences) that satisfy a Toeplitz matrix eigenvalue equation given by

$$\sum_{m=0}^{N-1} \frac{\sin 2\pi W(n-m)}{\pi(n-m)} v_m^{(k)}(N, W) = \lambda_k(N, W) v_n^{(k)}(N, W) \quad (4.3)$$

where N is the number of data points,

W is the bandwidth, which is in the order of $1/N$,

k is the column number,

$v^{(k)}$ are the eigenvectors that correspond to the windows to be used to maximize the energy concentration within the specified bandwidth, W , and

λ_k are the eigenvalues that give us an estimate of the leakage that the data set incurs for the window, $v^{(k)}$.

We only need the first $K=2NW$ terms with the largest eigenvalues, but Thomson suggests that we use the first $2NW-1$ terms to minimize leakage due to the higher order window leakage.

The complex spectrum, $S(t)$ (t is the travel time to the target), can be estimated as follows

$$X_k(t) = IFFT\{x(f) \times v^{(k)}\} \quad (4.4)$$

$$S(t) = \frac{1}{K} \sum_{k=0}^{K-1} \frac{1}{\lambda_k} X_k(t) \quad . \quad (4.5)$$

where $x(f)$ is the raw step-frequency data, and

$X_k(t)$ is the individual spectrum estimate corresponding to the data window $v^{(k)}$.

4.1 Coherent Noise Reduction (CNR)

Since the data were collected in a single antenna mode, the spectrum will include the reflection from the antenna and feedthrough (figure 4.3). These signals are usually much stronger than those of the target, especially at higher incidence angles ($>10^\circ$). At these angles, the return from the ice is barely visible.

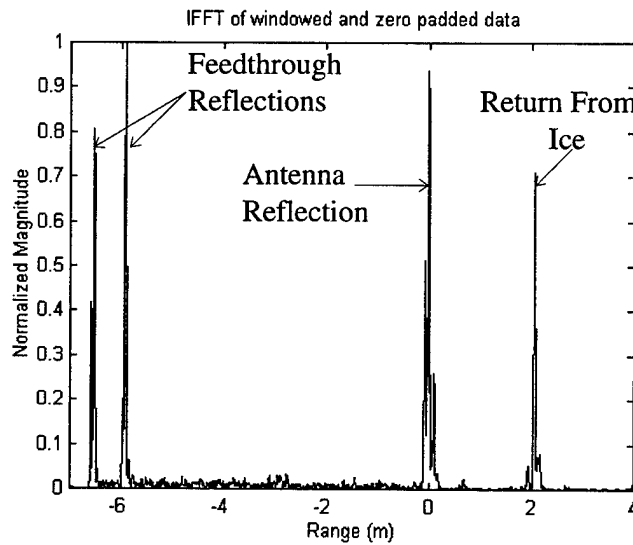


Figure 4.3. Impulse response of ice.

Usually, there are two ways that these unwanted reflections are reduced. The first way is to subtract coherently the background return from that of the ice. This can be accomplished by pointing the antenna to the sky, but we could not do this because of the limited extension range of the actuator. The second way is to implement a hardware range gate to suppress these unwanted reflections, but this technique requires very fast switches for short ranges. We tried range gating with a commercial hardware range gate, the LINTEK Range Gate, but we were unsuccessful using this hardware. To reduce the feedthrough signals we employed the coherent noise reduction (CNR) technique [Beaven, 1995]. The primary assumption of this technique is that the phase of the return from a distributed target varies randomly from one sample to another while the phase of the feedthrough signals remains constant. CNR is carried out by coherently averaging several independent samples at each angle and subtracting the average from each sample. Coherent averaging reduces the return from the target because of the varying phase and gives us an estimate of the system clutter, which is coherent. If we have N independent samples ($V_1 \dots V_N$), CNR applied to V_1 is simply

$$V_{1CNR} = V_1 - \frac{1}{N} \sum_{i=1}^N V_i \quad (4.6)$$

Figure 4.4 shows an example of CNR done on a 15° return from pancake ice.

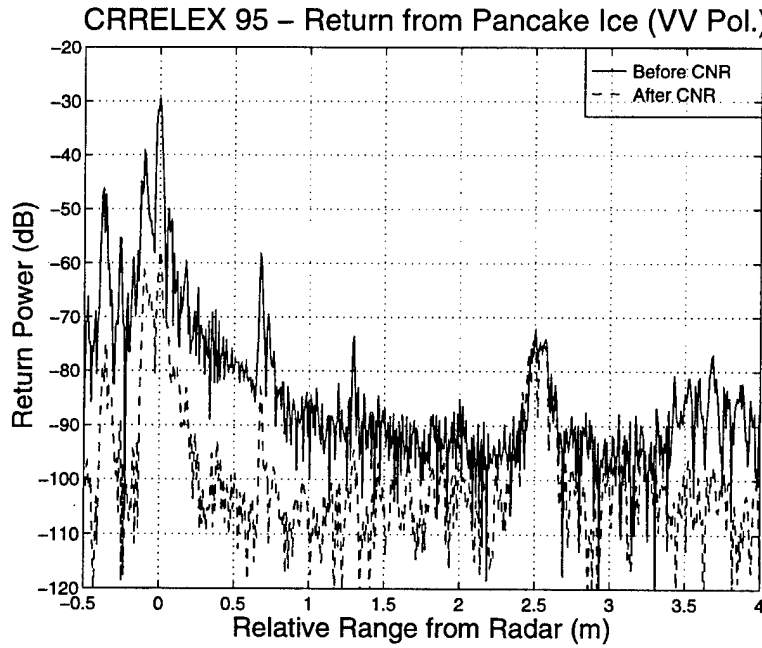


Figure 4.4. Result of CNR on pancake ice at 15° incidence angle. These data were collected using the plane-wave system during the CRRELEX '95 experiment.

4.2 Filtering & FFT

To isolate the ice return from other signals in the range domain, we needed to design a narrow-band bandpass digital filter. We designed the narrow-band filter using Thomson's Multiple Windows to obtain the maximum concentration of energy within a specified bandwidth, W . The filter, H , is obtained by taking the FFT of the windows for the designed bandwidth, W , dividing them by the leakage factor and summing them. The steps are as follows

$$F_k = \text{FFT}\{v^{(k)}\} \quad (4.7)$$

$$H = \frac{1}{K} \sum_{k=0}^{K-1} \frac{1}{\lambda_k} F_k \quad . \quad (4.8)$$

The following is the filtering sequence used to extract the wideband response of the return.

- 1) From the spectrum of the signal determine the return associated with the target and synthesize a Thomson's bandpass filter centered on the return from the ice.
- 2) The FFT of the filtered signal will give us the frequency response of the ice return. The drawback to this response is the effect of the filter's transient response to the range-domain band edge, where the transfer-function response is assumed to go abruptly to zero.
- 3) To reduce the ringing effect, we created a correction factor for the frequency response [Higgins, 1990]. This is done by simulating the step-frequency data with a reflection coefficient of one with the range being set equal to that of the target. The same process of windowing, zero padding and IFFT performed on the measured data is repeated for the simulated data. The filter used for the simulated data should be identical to that of the target. The FFT of this filtered signal is the correction factor that is divided by the frequency response of the target. Figure 4.5 (a) and (b) shows the effects of filtering simulated data with and without the correction factor. The filter's passband passed only 4 range cells ($4 * \Delta R$). The corrected frequency response has about 2% error at the edges. Notice the ringing effect in the beginning of the uncorrected filtered response.

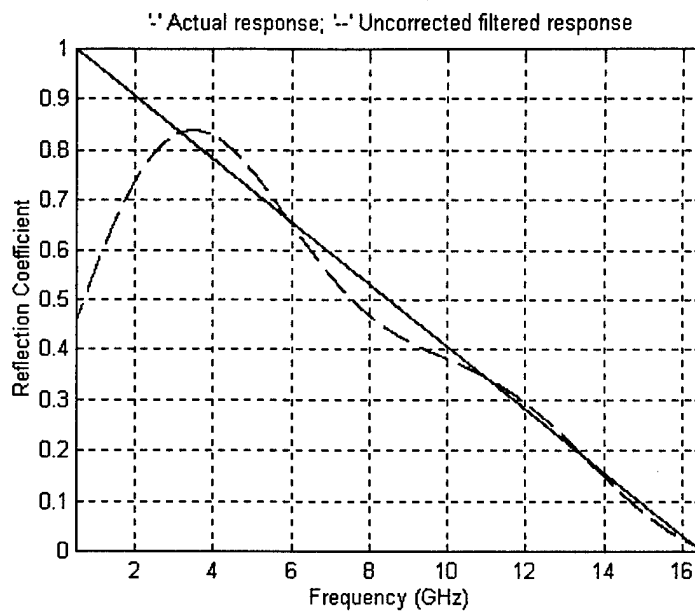


Figure 4.5(a). Frequency response of filtered data using Thomson's filter. (— = actual response; - - - = uncorrected filtered response).

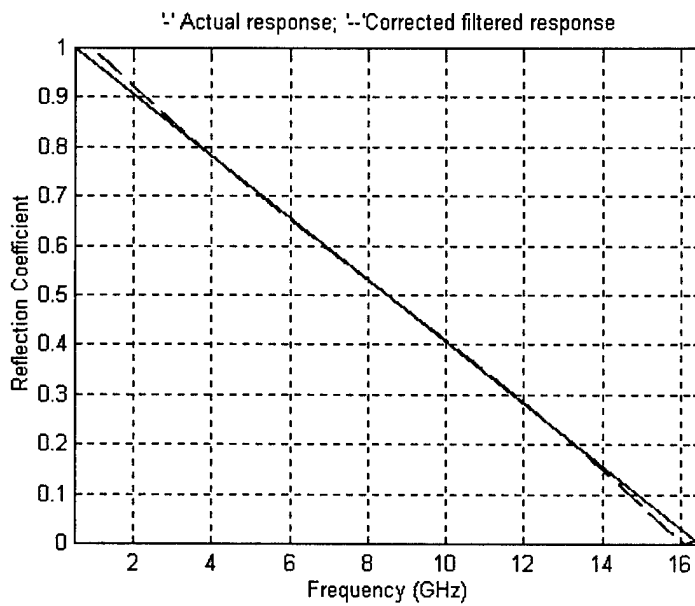


Figure 4.5(b). Filtered data with correction factor applied (— = actual response; - - - = corrected filtered response).

The effectiveness of the correction is dependent on the width of the filter passband. The larger the filter passband, the more accurate will be our frequency response, but widening the filter may include spurious responses from our measured data. For low incidence angles (0° - 10°), two to four range cells in the passband are sufficient to obtain the frequency response. For higher incidence angles, a wider passband should be used to include the returns from the larger illuminated area. The corrected frequency response of the target, $P_r(f)$, is used in (4.1) to compute the backscattering coefficient. Figure 4.6 shows an example of the frequency response, $P_r(f)$, of the return from pancake ice at 0° .

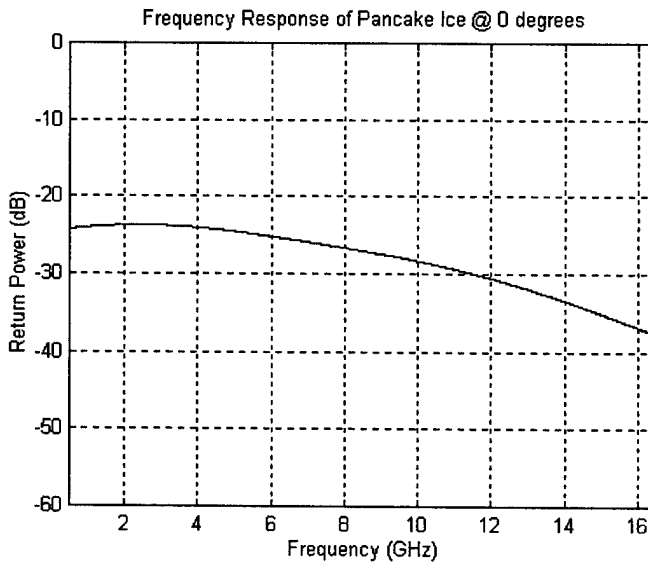


Figure 4.6. Uncalibrated return power as a function of frequency for pancake ice at 0° .

5. CRRELEX Results

The results of the CRREL experiments are presented in three parts. The first part consists of a few impulse response plots of the various ice types; namely, bare ice and snow-covered ice at a few angles. The second part consists of angular responses of the scattering coefficients for bare ice, snow-covered ice and pancake ice types at C band and Ku band. A comparison between the scattering coefficients obtained using the plane-wave and the spherical-wave antennas are shown here. Comparison with field measurements for pancake ice is also made in this section. The third part consists of frequency responses of the scattering coefficients at various incidence angles. A comparison between the measured and theoretical scattering response of bare ice at 5° , 10° , 15° , 20° and 30° is also shown here.

5.1 Impulse Response

Figure 5.1 shows the typical response from bare ice at nadir. The return from smooth bare ice at nadir resembles a delta function. There is a spurious response 8 cm after the ice reflection. This could be due to the system response since a similar response is also observed from the snow-covered ice. As the incidence angle is increased to 5° , the return power drops by almost 30 dB (figure 5.2). This demonstrates the excellent angular resolution that we are able to achieve with our system.

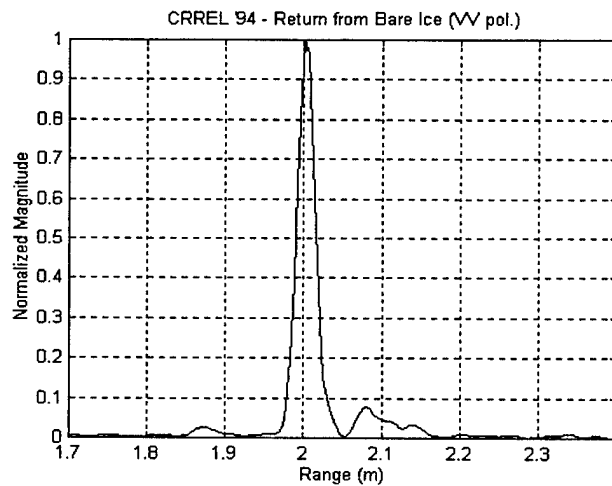


Figure 5.1. Return from bare ice at 0° .

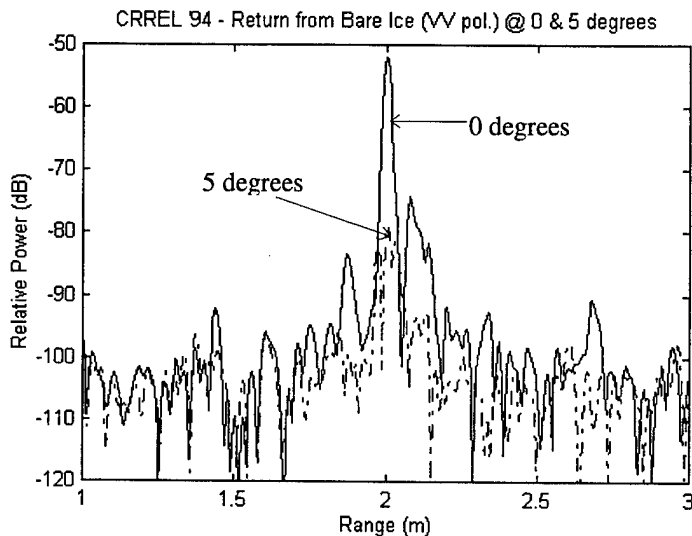


Figure 5.2. Return from bare ice at 0° and 5° .

Figure 5.3 demonstrates the excellent resolving capability of the plane-wave system. Notice the clear reflections from the air/snow and the snow/ice interfaces, which are about 5 cm apart. The reflection from the snow/ice interface is about seven times higher than that from the air/snow interface. This is due to the higher dielectric contrast between snow and saline ice than between snow and air.

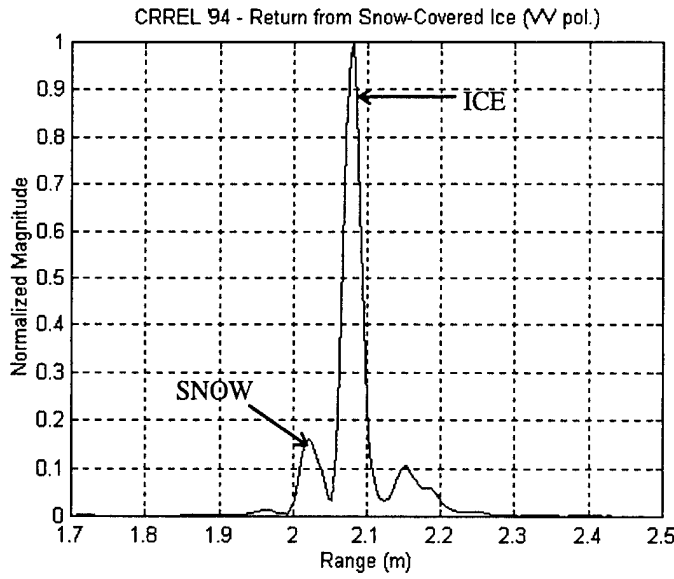


Figure 5.3. Return from snow-covered ice at 0° .

We used a resonant probe [Smith and King, 1974] to measure the dielectric constants of ice and snow. The resonant frequency of the probe was measured in free space and the medium. The relationship between the resonant frequency of the probe in the medium and its dielectric constant is given by

$$\frac{\epsilon_{med}}{\epsilon_{air}} = \left(\frac{f_{air}}{f_{med}} \right)^2 \quad (5.1)$$

where ϵ_{med} & ϵ_{air} are the dielectric constants of the medium and air, respectively, and f_{med} & f_{air} are the resonant frequencies of the probe in the medium and air, respectively.

The dielectric constants of ice and snow were measured to be 3.5 and 1.17, respectively. The relationship between the reflection coefficient and the dielectric constant of a material is given by

$$\Gamma = \frac{\sqrt{\epsilon_2/\epsilon_1} - 1}{\sqrt{\epsilon_2/\epsilon_1} + 1} \quad (5.2)$$

where Γ is the reflection coefficient at the dielectric interface and ϵ_1 & ϵ_2 are the dielectric constant of medium 1 and medium 2, respectively.

The reflection coefficients at the snow/ice interface and air/snow interface were found to be 0.266 and 0.0406, respectively. The ratio of the reflection coefficient from the ice to snow is 6.56:1. This agrees with our measured result shown in figure 5.3.

5.2 Angular Scattering Response

The scattering responses were computed and calibrated to a metal sphere with a radar cross section, σ_{cal} , of -13.9 dBm² over the entire frequency range.

Figure 5.4 illustrates how wide-beam (spherical-wave) antennas corrupt the scattering response from bare ice at near vertical incidence. The scattering coefficient obtained using the plane-wave system at 5° is 25 dB lower than that obtained using the conventional system. The results of the horn antenna are corrupted by scattering from vertical until the incidence angle increases to about 20°. The data collected using the horn antenna needs to be corrected for the large beamwidth in order to obtain the correct angular response. This result confirms the superiority of the plane-wave system over conventional systems for measuring the angular dependence of the scattering response for vertical incidence.

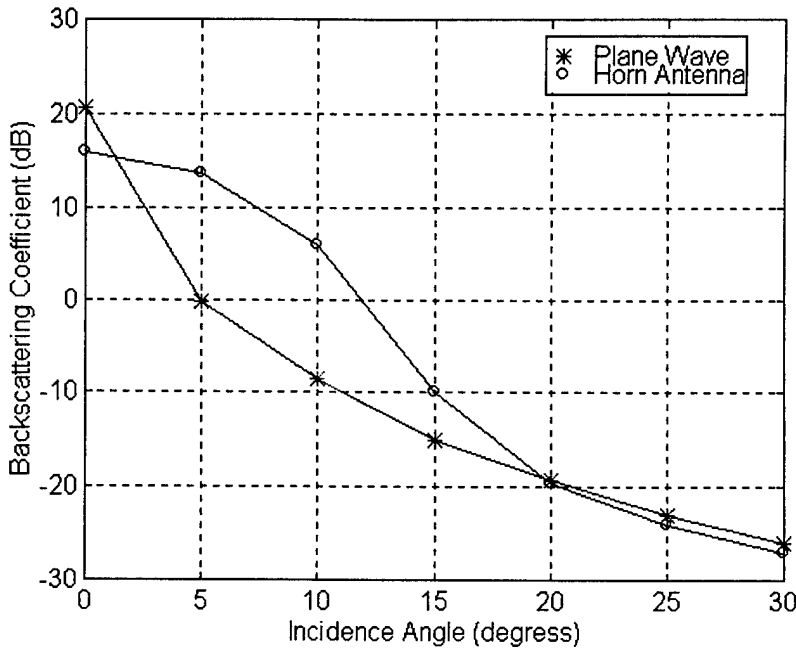


Figure 5.4. Comparison of backscattering coefficient from bare ice obtained using plane-wave and spherical-wave antennas at Ku band.

Figures 5.5 and 5.6 below show the angular response of several ice types at C band and Ku band, respectively. From the plots above we can see that the scattering for pancake ice is higher than bare ice for angles greater than zero. The results show that there is more incoherent scattering from pancake ice because of its rougher surface. The scattering from snow-covered ice is slightly higher than that from bare ice because of the slightly rougher surface. We can also see for the three ice types that surface scattering may dominate, at least until 30° , because of the scattering coefficient falloff with angle.

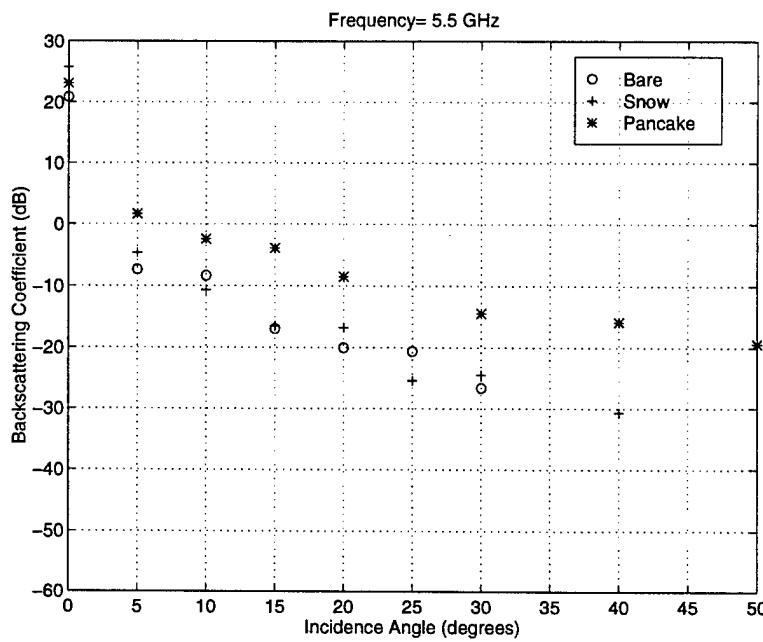


Figure 5.5. Angular response of bare ice, snow-covered ice and pancake ice at C band.

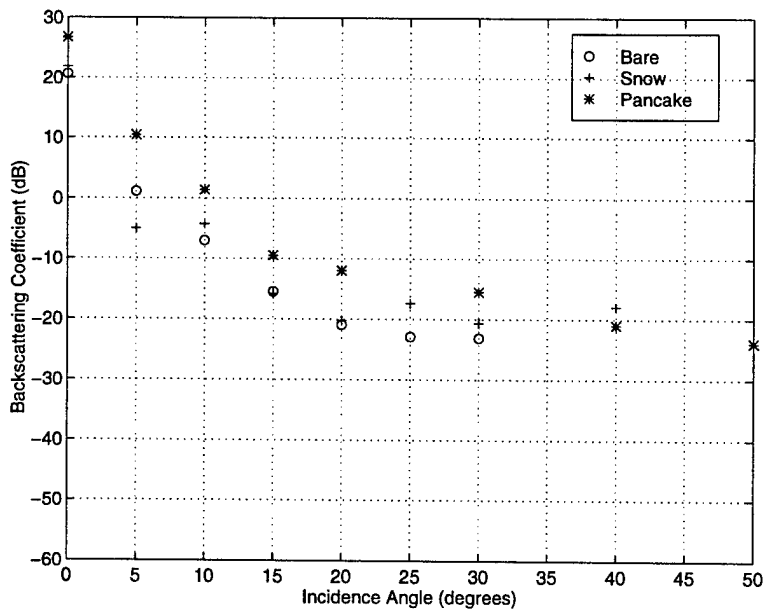


Figure 5.6. Angular response of bare ice, snow-covered ice and pancake ice at Ku band.

Figure 5.7 shows the agreement between field [Beaven, 1992] and laboratory backscatter characteristics of pancake ice at 35° .

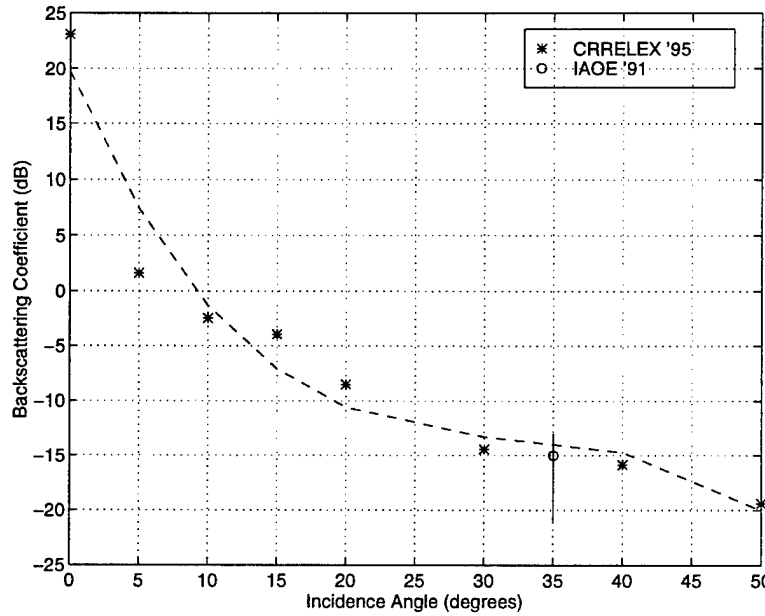


Figure 5.7. Pancake ice comparison at C Band.

5.3 Frequency Scattering Response

At 0° (figure 5.8), we see that scattering from pancake ice is increasing with frequency. The scattering level increased from 21-29 dB as the frequency was increased from 2-15 GHz. When the frequency is increased, the surface seen by the radar becomes rougher. This would mean that the scattering in the specular direction will begin to reduce and the scattering will begin to increase in other directions. The scattering in other directions are called the incoherent components. From figure 5.8, we can infer that at the initial frequency of 2 GHz, the incoherent components have been

dominating for the pancake ice and, as the frequency is increased, we get an increase in scattering from the incoherent components. As for the snow-covered ice, it can be observed that the scattering decreased from 25-19 dB as the frequency was increased from 3.5-16.5 GHz. From this result we can infer that the coherent component has been dominating at the initial frequency of 3.5 GHz and as the frequency is increased, we get a decrease in scattering from the coherent component and an increase in scattering from the incoherent components. The higher scattering at the initial frequencies could be due to wet snow at the snow-ice interface. As for the bare ice, there is no significant change in the scattering level across the frequency range, which means that there is only a dominant coherent component. To explain the relative scattering levels of these three ice types, more modeling effort is required to determine the contribution from the incoherent and coherent components.

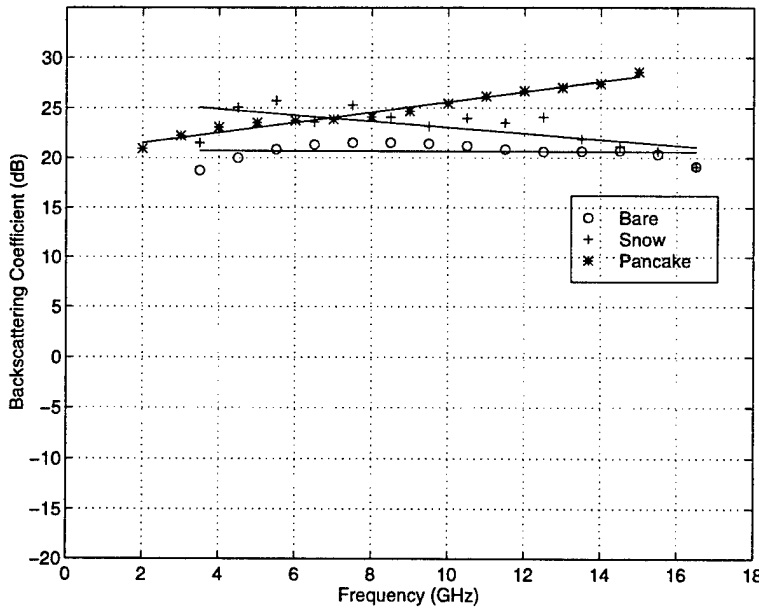


Figure 5.8. Frequency response of bare ice, snow-covered ice and pancake ice at 0° .

When the incidence angle is increased to 5° (figure 5.9), there is a 15- to 20-dB drop in the scattering coefficient of pancake ice and about a 25- to 30-dB drop in the scattering coefficient of bare ice and snow-covered ice. The large drop in the scattering level is due to the reduction in coherent scattering. The high scattering coefficient at the initial frequency is due to the coherent contribution of the ice. This is due to the larger beamwidth of the radiating pattern at the lower frequencies. The scattering level for pancake ice increased as a function of frequency. This is an indication of dominant incoherent scattering.

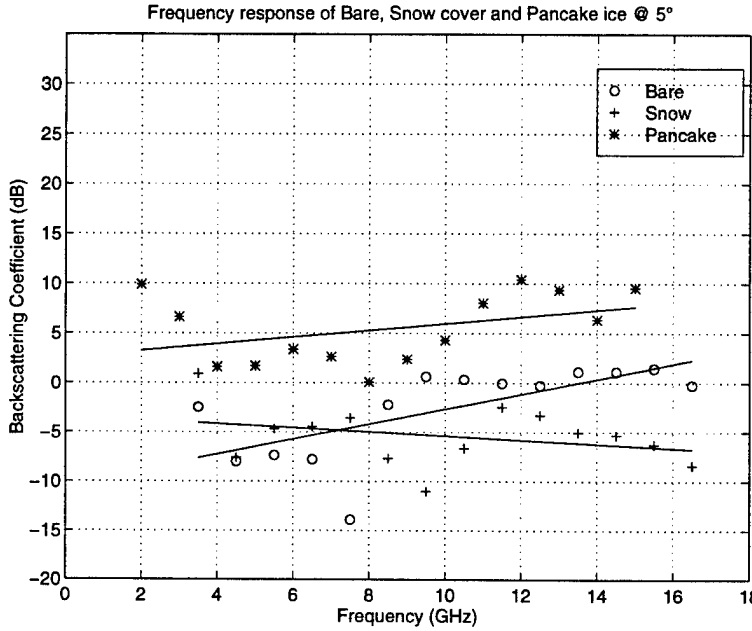


Figure 5.9. Frequency response of bare ice, snow-covered ice and pancake ice at 5°.

The results for the bare ice measurements at 5° and beyond were compared to theory. The coherent component was computed using Fung and Eom's [1983] model and the incoherent component was computed using the integral equation method (IEM) model [Fung, 1994]. The solution to determine the coherent contribution, σ_c^o , is given by Fung and Eom as

$$\sigma_c^o = \frac{\Gamma_p}{B^2} \exp(-4k^2\sigma_h^2) \exp(-\theta^2 / B^2) \quad (5.3)$$

where Γ_p is the reflection coefficient for polarization p (either H or V),

θ is the incidence angle,

k is the wavenumber,

σ_h is the rms roughness, and

B is given by

$$B^2 = \frac{1}{(kh\beta)^2} + \left(\frac{\beta}{2}\right)^2 \quad (5.4)$$

where β is the one-sided beamwidth and

h is the range to the scatterer.

The incoherent component, σ_{inc}^o , using the IEM model is given as

$$\sigma_{inc}^o = \frac{k^2}{2} \exp(-2k_z^2 \sigma^2) \sum_{n=1}^{\infty} |I_{vv}^n|^2 \frac{W^{(n)}(-2k_x, 0)}{n!} \quad (5.5)$$

where $k_z = k \cos \theta$, $k_x = k \sin \theta$,

$$I_{vv}^n = (2k_z \sigma)^2 f_{vv} \exp(-k_z^2 \sigma^2) + \frac{(k_z \sigma)^n [F_{vv}(-k_x, 0) + F_{vv}(-k_x, 0)]}{2} \quad (5.6)$$

and the symbol $W^{(n)}(-2k_x, 0)$ is the Fourier transform of the nth power of the surface correlation function. Other symbols are given in Appendix 2A of Fung, 1994.

The theoretical scattering coefficient, σ_{vv}^o , is given by

$$\sigma_{vv}^o = \sigma_c^o + \sigma_{inc}^o \quad (5.7)$$

The parameters used for these models are given in Table 5.1.

Table 5.1. Model parameters for bare saline ice

Parameter	Value
rms roughness, σ_h	1.0 mm
correlation length, L_c	2.2 cm
dielectric constant, ϵ_r	3.38-j0.22
One-sided beamwidth @ 3 GHz	2.3°
Equivalent spherical source range, h	9.3 m

The beamwidth and range are factors only for the coherent contribution case.

The equivalent spherical source range was calculated using the radius of the illuminated area from figure 4.1(a-d) and the beamwidth. From figure 5.10, we can determine h using the trigonometric relation

$$h = \frac{r}{\tan(\beta)} \quad (5.8)$$

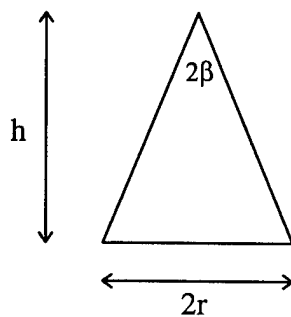


Figure 5.10. Range calculation for equivalent spherical source.

To determine the beamwidth of the radiating pattern, we measured the impulse response of the plane-wave system using a mesh screen at 0° , 0.5° , 1.0° , 1.5° , 2.0° and 5.0° . The power return from the mesh screen at angles beyond 0° is due to the coherent component. From the coherent returns at the various incidence angles, we can estimate the radiation pattern of the antenna. Figure 5.11 shows the one-sided, two-way radiating pattern of the plane-wave antenna at 3 GHz, which has been fitted with a Gaussian curve. The one-sided beamwidth for the one-way pattern is the -6dB point of the two-way radiating pattern. At 3 GHz, this corresponds to about 2.3° .

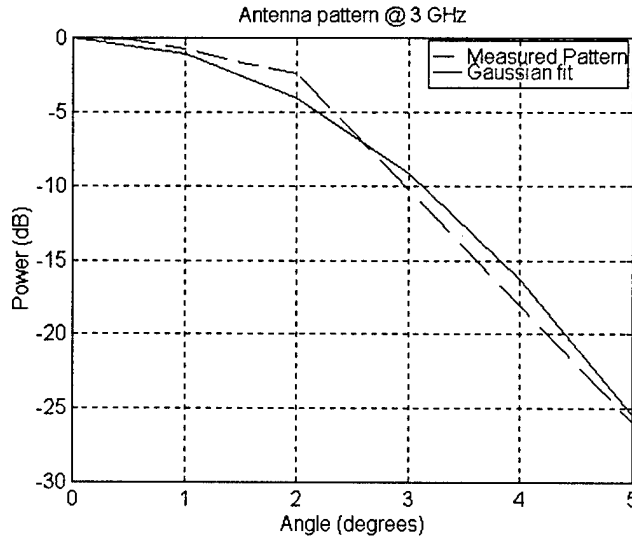


Figure 5.11. Radiating pattern of the plane-wave antenna at 3 GHz.

Figure 5.12 shows the comparison between the theoretical scattering values and the measured values of bare saline ice at 5° . From this figure we see that the coherent

component is dominating the scattering source until about 6 GHz and the incoherent scattering begins to dominate beyond 6 GHz.

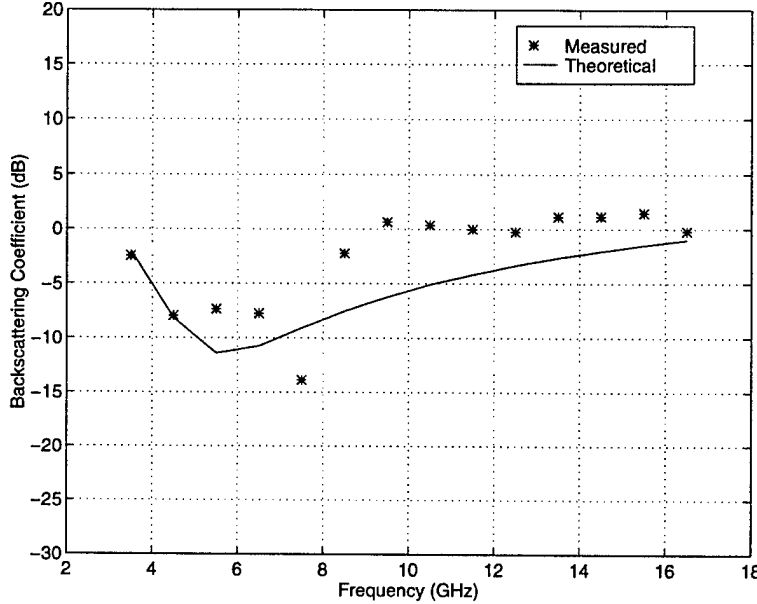


Figure 5.12. Comparison between theoretical and measured scattering of bare ice at 5° .

At 30° (figure 5.13), the scattering level for bare ice and snow-covered ice increased by about 12 dB with increasing frequency. This increase corresponds to an increase in incoherent scattering. The scattering from pancake ice also exhibits a similar behavior but with a higher scattering level due to its rougher surface.

Figure 5.14 shows the scattering comparison between the theoretical scattering values and the measured values of bare saline ice at 30° .

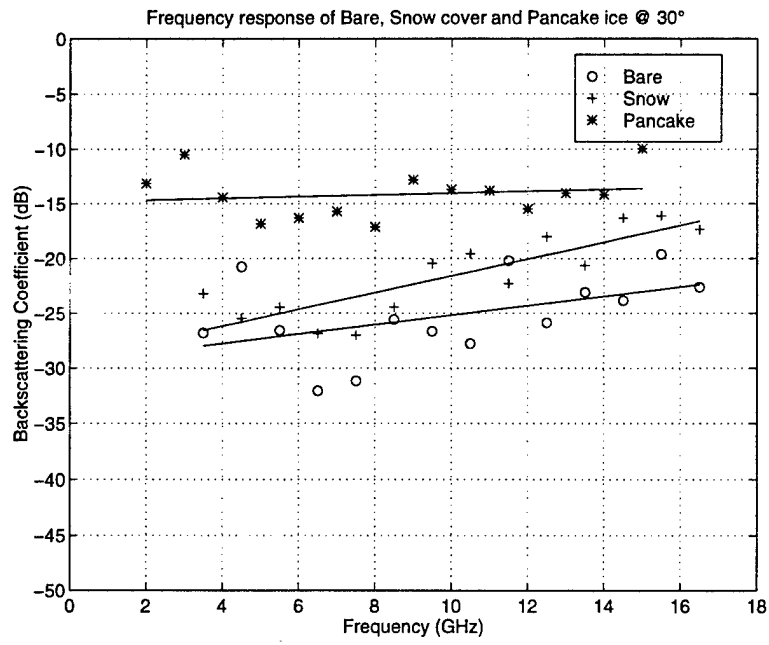


Figure 5.13. Frequency response of bare ice, snow-covered ice and pancake ice at 30° .

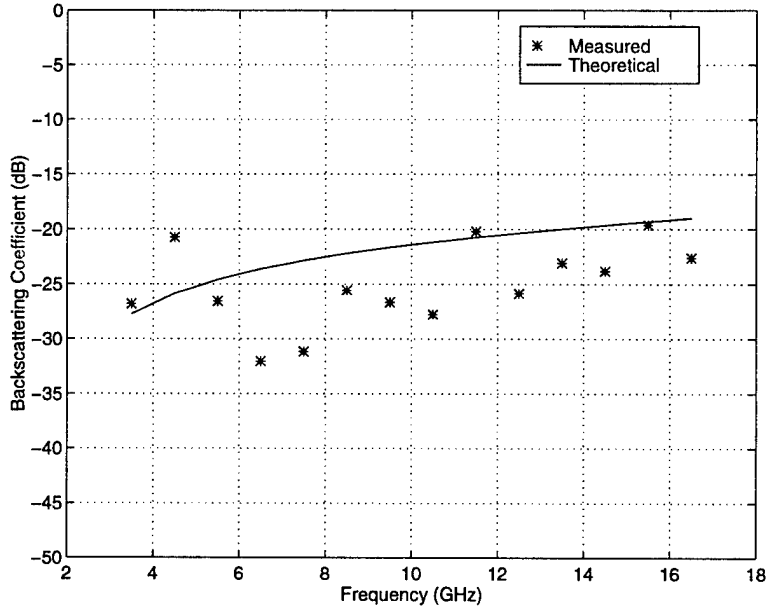


Figure 5.14. Comparison between theoretical and measured scattering of bare ice at 30° .

Figures 5.15-5.17 show the comparison between the theoretical and measured values of bare ice at 10° , 15° and 20° . We believe that the discrepancies at the initial frequencies at these angles are due to the coherent component from the sidelobes of the radiating pattern.

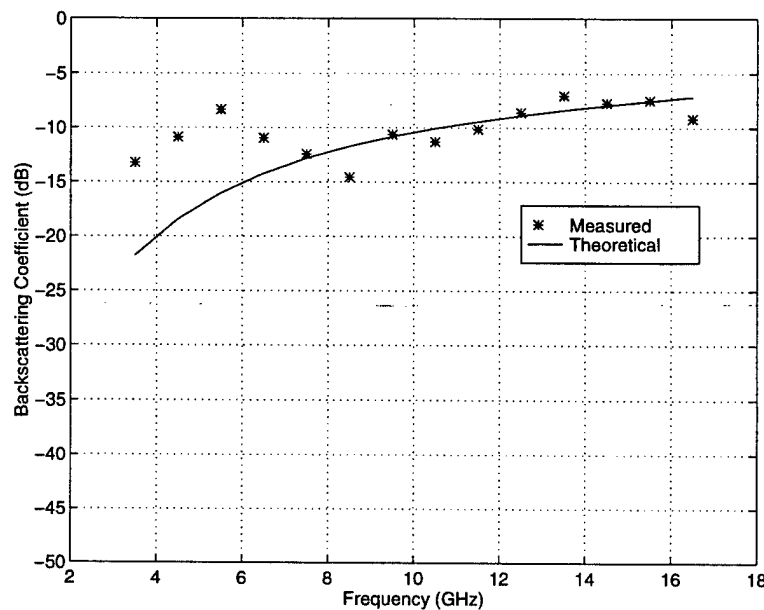


Figure 5.15. Comparison between theoretical and measured scattering of bare ice at 10° .

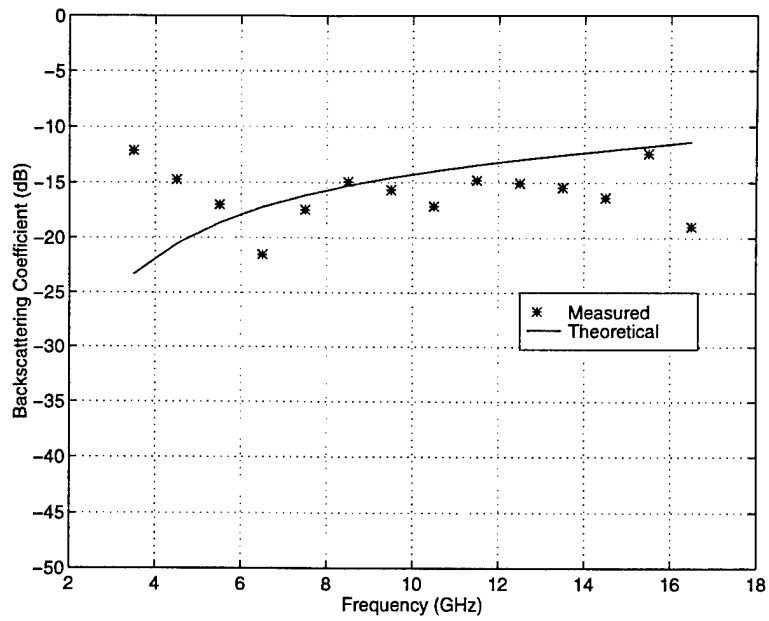


Figure 5.16. Comparison between theoretical and measured scattering of bare ice at 15° .

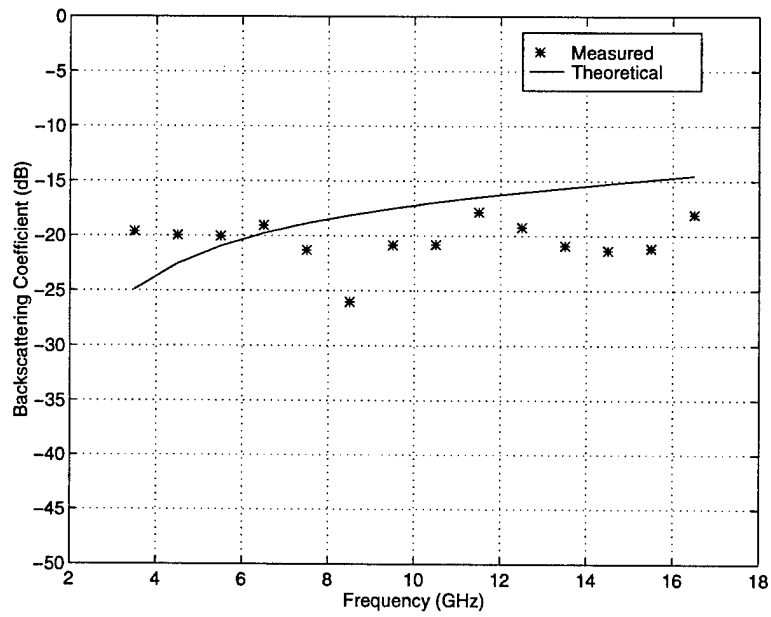


Figure 5.17. Comparison between theoretical and measured scattering of bare ice at 20° .

6. Conclusions and Future Work

An ultra-wideband radar and a plane-wave antenna have been used to measure the high-resolution scattering response of bare saline ice, snow-covered ice and pancake ice at the US Army Cold Regions Research and Engineering Laboratory (CRREL) during the 1994 and 1995 winter seasons.

We have developed signal processing techniques using Thomson's Multiple Windows to estimate the high-resolution spectrum and to extract the wideband response of the signal. We have shown how the ringing effect associated with narrowband filters can be reduced by using a correction factor.

The results of our measurements show the excellent spatial and angular resolution that can be achieved with the plane-wave system. The scattering coefficients obtained using the plane-wave system show that surface scattering dominates at least until 30°. At 0°, the scattering from bare ice stayed fairly constant with about 1- to 2-dB variation across the 2- to 18-GHz frequency range, while the scattering from pancake ice increased from 21 to 29 dB with increasing frequency. On the other hand, the scattering from snow-covered ice decreased from 25 to 19 dB with increasing frequency. This shows that there is more contribution from incoherent components for pancake ice at higher frequencies, while for snow-covered ice there is less contribution from the coherent component at the higher frequencies. At 5° incidence angle, we can see that the coherent component is still dominating up to 6 GHz, after which the incoherent component begins to dominate. At 30° incidence angle, the scattering

increased as a function of frequency, which is an indication of dominant incoherent scattering. With increasing incidence angle, the scattering level dropped. This is an indication of dominant surface scattering. Field measurement of pancake ice at 35° shows agreement with laboratory measurements.

We need to ascertain the radiating pattern of the antenna beyond 5° to determine if there are any coherent sources of scattering at these angles. We also need to do modeling on the different ice types to determine the relative surface and volume contributions. There is also a potential for using a focussed beam for better penetration and probing of surface roughness over the ice.

REFERENCES

- Beaven, S., Radar Backscatter Measurements from Simulated Sea Ice and Arctic Sea Ice during the Fall Freeze-up, MS Thesis, University of Kansas, 1992.
- Beaven, S., Sea Ice Radar Backscatter Modeling, Measurements, and the Fusion of Active and Passive Microwave Data, Ph.D. Dissertation, University of Kansas, 1995.
- Fung, A.K., *Microwave Scattering and Emission Models and Their Applications*, Artech House, Norwood, Massachusetts, 1994.
- Fung, A.K. and H.J. Eom, Coherent scattering of a spherical wave from an irregular surface, *IEEE Transactions on Antennas and Propagation*, vol. AP-31, pp. 68-72, Jan 1983.
- Gogineni, S.P., K. Jezek, L. Peters, J. Young, S. Beaven, and E. Nassar, Application of plane waves for accurate measurement of microwave scattering from geophysical surfaces, *IEEE Transactions on Geoscience and Remote Sensing*, vol. 33, no. 3, pp. 627-633, 1995.
- Higgins, R.J., *Digital Signal Processing in VLSI*, Prentice Hall, Englewood Cliffs, New Jersey, 1990.
- Izuka, K., A.P. Freundorfer, K.H. Wu, H. Mori, H. Ogura, and V.K. Nguyen, Step-frequency radar, *Journal of Applied Physics*, vol. 56, no. 9, pp. 2572-2583, 1984.

- Nassar, E.M., Aperture Distributions Generated by Transmission Line Feed Structures, MS Thesis, The Ohio State University, 1992.
- Smith, G.S., and R.W.P. King, The resonant linear antenna as a probe for measuring in situ electrical properties of geological media, *Journal of Geophysical Research*, vol. 79, pp. 2623-2628, 1974.
- Thomson, D.J., Spectrum estimation and harmonic analysis, *Proceedings of the IEEE*, vol. 70, pp. 1055-1096, Sep. 1982.

BIBLIOGRAPHY

- Bayram, M., Multiple Window Time-Frequency Analysis, MS Thesis, Rice University, 1996.
- Beaven, S., and S.P. Gogineni, Shipborne radar backscatter measurements from Arctic sea ice during the fall freeze-up, *Remote Sensing Reviews*, vol. 9, nos. 1-2, pp. 3-25, 1994.
- Haykin, S., and A. Steinhardt, *Adaptive Radar Detection and Estimation*, Wiley, New York, 1992.
- Jezek, K., S.P. Gogineni, L. Peters, J. Young, S. Beaven, E. Nassar, and I. Zabel, Microwave scattering from saline ice using plane wave illumination, *Digest IGARSS'94*, pp. 493-495, Pasadena, California, August 8-12, 1994.
- Kanagaratnam, P., High-Resolution Radar Backscatter From Sea Ice And Range-Gated Step-Frequency Radar Using The FM-CW Concept, MS Thesis, University of Kansas, December 1995.

REPORT DOCUMENTATION PAGE

OMB NO. 0704-0188

Please provide the Bureau for the correction of information. A reasonable time estimate to average 1 hour per responder, including the time for reviewing instructions, searching existing cold storage databases and maintaining the data needed, and completing and returning the correction of information. Send comments regarding this Bureau's estimate or any other aspect of the collection of information, including suggestions for reducing the burden, to Washington Headquarters Services, Directorate for Information Operations and Reports, 1215 Jefferson Davis Highway, Suite 1204, Arlington, VA 22202-4302, and to the Office of Management and Budget, Paperwork Reduction Project (0704-0188), Washington, DC 20503.

1. AGENCY USE ONLY (Leave blank)	2. REPORT DATE	3. REPORT TYPE AND DATES COVERED	
	July 1997	experiments during '94 & '95 winter seasons Tech. Report,	
4. TITLE AND SUBTITLE		5. FUNDING NUMBERS	
Ultra-wideband radar measurements over bare, snow-covered and pancake ice		ONR doc. no. N00014-96-1-0219	
6. AUTHOR(S)			
P. Kanagaratnam, S. Gogineni, K. Jezek, L. Peters, J. Young & I. Zabel			
7. PERFORMING ORGANIZATION NAME(S) AND ADDRESS(ES)		8. PERFORMING ORGANIZATION REPORT NUMBER	
Radar Systems and Remote Sensing Laboratory University of Kansas Center for Research, Inc. 2291 Irving Hill Road Lawrence KS 66045-2969		RSL TR 12100-1	
9. SPONSORING/MONITORING AGENCY NAME(S) AND ADDRESS(ES)		10. SPONSORING/MONITORING AGENCY REPORT NUMBER	
Office of Naval Research Arlington VA 22217-5660 and Regional Office San Diego 4520 Executive Dr, Suite 300 San Diego CA 92121-3019		?	
11. SUPPLEMENTARY NOTES			
12a. DISTRIBUTION/AVAILABILITY STATEMENT		12b. DISTRIBUTION CODE	
Approved for public release.		?	
13. ABSTRACT (Maximum 200 words)			
An ultra-wideband radar and a plane-wave antenna have been used to measure the high resolution scattering response of bare saline ice, snow-covered ice and pancake ice during the winter seasons of 1994 and 1995 at the US Army Cold Regions Research and Engineering Laboratory (CRREL). The objectives of these experiments were to study various mechanisms for simulating roughness and to understand scattering mechanisms better.			
These backscatter measurements were made at 2-18 GHz and 0.5-16.5 GHz during the 1994 and 1995 experiments, respectively, and were made for incidence angles ranging from 0° to 55°. These broadband measurements provide a vigorous test for models at many frequencies using a single system instead of many single frequency systems.			
14. SUBJECT TERMS		15. NUMBER OF PAGES	
		40	
		16. PRICE CODE	
17. SECURITY CLASSIFICATION OF REPORT	18. SECURITY CLASSIFICATION OF THIS PAGE	19. SECURITY CLASSIFICATION OF ABSTRACT	20. LIMITATION OF ABST